

Analysis of hydrogen-rich magnetic white dwarfs detected in the Sloan Digital Sky Survey

B. Külebi¹, S. Jordan¹, F. Euchner², B. Gänsicke³, and H. Hirsch⁴

¹ Astronomisches Rechen-Institut, Zentrum für Astronomie der Universität Heidelberg, Mönchhofstrasse 12-14, D-69120 Heidelberg, Germany

² Swiss Seismological Service, ETH Zurich, Sonneggstrasse 5, CH-8092 Zurich, Switzerland

³ Department of Physics, University of Warwick, CV4 7AL Coventry, United Kingdom

⁴ Dr.-Reemis-Sternwarte, Sternwartstrasse 7, D-96049 Bamberg, Germany

Preprint online version: April 25, 2022

ABSTRACT

Context. A large number of newly discovered magnetic white dwarfs in the SDSS have so far only been analysed by visual comparison of the observations with relatively simple models for the radiation transport in a magnetised stellar atmosphere.

Aims. We model the structure of the surface magnetic fields of the hydrogen-rich white dwarfs in the SDSS.

Methods. We have calculated a grid of state-of-the-art theoretical optical spectra of hydrogen-rich magnetic white dwarfs with magnetic field strengths between 1 MG and 1200 MG for different angles between the magnetic field vector and the line of sight, and for effective temperatures between 7000 K and 50000 K. We used a least-squares minimization scheme with an evolutionary algorithm in order to find the magnetic field geometry best fitting the observed data. We used simple centered dipoles or dipoles which were shifted along the dipole axis to model the coadded SDSS fiber spectrum of each object.

Results. We have analysed the spectra of all known magnetic DAs from the SDSS (97 previously published plus 44 newly discovered) and also investigated the statistical properties of magnetic field geometries of this sample.

Conclusions. The total number of known magnetic white dwarfs already more than tripled by the SDSS and more objects are expected from a more systematic search. The magnetic fields span a range between ≈ 1 and 900 MG. Our results further support the claim that Ap/Bp population is insufficient in generating the numbers and field strength distributions of the observed MWDs, and either another source of progenitor types or binary evolution is needed. Moreover clear indications for non-centered dipoles exist in about $\sim 50\%$ of the objects which is consistent with the magnetic field distribution observed in Ap/Bp stars.

Key words. stars: white dwarfs – stars: magnetic fields – stars: atmospheres

1. Introduction

White dwarfs with magnetic fields between 10^4 and 10^9 G are thought to represent more than 10% of the total population of white dwarfs (Liebert et al. 2003). The Sloan Digital Sky Survey (SDSS), the largest spectroscopic survey carried out to date, has discovered thousands of new white dwarfs, among them 102 with magnetic fields (MWDs) (Gänsicke et al. 2002; Schmidt et al. 2003; Vanlandingham et al. 2005). By Data Release 3 (DR3) the number of known magnetic white dwarfs increased from 65 (Wickramasinghe & Ferrario 2000; Jordan 2001) to 167 (Kawka et al. 2007). The first seven magnetic DAs (DAHs) uncovered from SDSS were identified visually in the area of the initial Early Data Release (EDR Gänsicke et al. 2002). Schmidt et al. (2003) added 46 objects in the DR1, 38 of them DAH plus three new magnetic DB (DBH), and five new MWDs showing metallic and molecular lines. Vanlandingham et al. (2005) reported on 49 additional new MWDs from the DR2 and DR3, specifically 46 new DAH, two new DQAs and one DQ with molecular bands.

Schmidt et al. (2003) and Vanlandingham et al. (2005) determined the field strengths and the inclinations of magnetic dipoles by comparing visually the observed spectra with model spectra. They have used an extension of the modeling method of

Latter et al. (1987) and accounted for the effect of the change of magnetic field strength on line depths and the variation of the field strength over the stellar surface for only the unpolarized radiation flux, namely Stokes parameter I. Their analyses with this simplified method of radiation transport resulted in dipolar field strengths for the SDSS MWDs between 1.5 MG and ~ 1000 MG. Including the pre-SDSS, formerly known MWDs their sample consisted of 111 MWDs, 97 were classified as DAHs.

In this work we present the re-analysis of SDSS DAHs, published by Gänsicke et al. (2002), Schmidt et al. (2003) and Vanlandingham et al. (2005), plus the analysis of 44 new ones from data up to DR7 (DR4 till DR7 were not systematically scanned for MWDs).

2. SDSS data

SDSS investigates five-band photometry of the Northern Galactic Polar Cap using the 2.5 meter telescope at Apache Point, New Mexico, with its special purpose instruments (Fukugita et al. 1996). Follow-up spectroscopy of many stars is also performed with the twin dual beam spectrographs (3900–6200 and 5800–9200 Å, $\lambda/\Delta\lambda \sim 1800$), in particular of blue objects like white dwarfs and hot subdwarfs (Harris et al. 2003; Kleinman et al. 2004). Since the energy distribution of strongly magnetic white dwarfs can differ from nonmagnetic

ones, MWDs are not only found in the SDSS color categories for white dwarfs or blue horizontal-branch stars, but may also fall into the color categories for quasars (QSOs), “serendipitous blue objects”, and hot subdwarfs. Based on their colors, objects are assigned to fibers for follow-up spectroscopic investigations (for spectroscopic target selection see Stoughton et al. 2002).

In order to identify magnetic white dwarfs from these samples, different techniques were used. From the sample of white dwarfs, selected by color cuts in the $u-g$ vs $g-r$ color-color diagram, Gänsicke et al. (2002) and Schmidt et al. (2003) used visual inspection. In the work by Vanlandingham et al. (2005) visual identification was augmented by the *autofit* process (Kleinman et al. 2004), which fits spectra and photometry of hydrogen and helium white dwarfs to theoretical models. In particular white dwarfs with magnetic fields above 3 MG, are flagged due to the poor χ^2 fits of the *autofit* process, therefore MWDs with weaker magnetic fields might be overlooked (Vanlandingham et al. 2005).

In addition to the data from the former SDSS MWD papers (DR1-DR3), we have analyzed new data of nineteen additional objects from the HYPERMUCHFUSS (HYPER velocity or Massive Unseen Companions of Hot Faint Under-luminous Stars Survey; see Tillich et al. 2009). This survey aims at the detection of high velocity under-luminous B stars and white dwarfs. The candidates were chosen by the selection criterion ($u-g$) <0.4 and ($g-r$) <0.1 and spectral fits were performed in order to determine the radial velocity. Some objects showed formally very high negative radial velocities (≤ -100 km/s) but turned out to be DAHs. The reason for this is that the higher-order Balmer lines of magnetic white dwarfs are systematically shifted to the blue, even at relatively small magnetic fields (≤ 20 MG) due to the quadratic Zeeman effect, mimicking a high radial velocity. Additionally, 34 DAHs were serendipitously found in the course of a visual inspection of blue stellar objects from DR7. The total number of DAHs from SDSS is likely to grow further once a systematic search through all DR7 spectra is carried out.

The one-dimensional spectra which we used in this work were generated by SDSS’s spectroscopic pipeline *spectro2d* and downloaded from the Data Archive Server.

3. Analysis

Our model spectra are calculated with a radiative transfer code for magnetized white dwarf atmospheres, which for a given temperature and pressure structure of a model atmosphere (T_{eff} , $\log g$) and a given magnetic field vector with respect to the line of sight and the normal on the surface of the star, calculates theoretical flux and polarization spectra (see Jordan 1992; Jordan & Schmidt 2003).

In order to increase efficiency, we pre-computed a three-dimensional grid of Stokes I and V (V spectrum not used due to the lack of polarization measurements) model spectra with effective temperature $7000 \text{ K} \leq T_{\text{eff}} \leq 50000 \text{ K}$ in 14 steps, magnetic field strength $1 \text{ MG} \leq B \leq 1.2 \text{ GG}$ in 1200 steps, and 17 different directions of ψ relative to the line of sight as the independent variables (9 entries, equally spaced in $\cos \psi$). All spectra were calculated for a surface gravity of $\log g = 8$. Since no polarization information is available from the SDSS, our analysis is limited to the flux spectra (Stokes parameter I). Limb darkening is accounted for by a simple linear scaling law (see Euchner et al. 2002).

The magnetic field geometry of the DAHs was determined with a modified version of the code developed by Euchner et al.

(2002). This code calculates the total flux (and circular polarization) spectra for an arbitrary magnetic field topology by adding up appropriately weighted model spectra for a large number of surface elements and then evaluating the goodness of fit. Magnetic field geometries are accounted for by multipole expansions of the scalar magnetic potential. The individual multipole components may be independently oriented with respect to the rotation axis of the white dwarf and offset with respect to its center, allowing in principle for rather complex surface field topologies. Additional free parameters are the white dwarf effective temperature and the inclination of the rotation axis with respect to the line of sight. Observed spectra can be fitted using an evolutionary algorithm (Rechenberg 1994) with a least-squares quality function.

Additionally to the Zeeman effect, Stark broadening has to be considered. For the case when the electric and magnetic fields are parallel Friedrich et al. (1994) have estimated the effect on stationary line components, which are transitions that vary slowly in wavelength for large intervals of magnetic field strengths. Stationary lines are more pronounced than non-stationary lines, since they are not smeared out extensively due to the variation of the magnetic field strength over the stellar surface.

However, no atomic data for hydrogen in the presence of both a magnetic and electric field are available for arbitrary strengths and arbitrary angles between two fields. Therefore, only a crude approximation (see Jordan 1992) is used in our model and systematic uncertainties are unavoidable, particularly in the low-field regime (≤ 5 MG) where the Stark effect dominates. Consequently, effective temperatures and surface gravities derived from fitting the Balmer lines alone are less reliable than in the case of non-magnetic white dwarfs. This may also result in disagreements with temperature estimates derived from the continuum slope.

Time-resolved analysis for rotating single magnetic white dwarfs was instrumental in determining rather complex field structures (e.g. VLT observations by Euchner et al. 2002, 2005, 2006). However this usually relies on the preliminary knowledge of period which is usually derived via photometry, separately. Although the individual SDSS fiber spectra exists with 15 minute exposure time, due to the lack of information on spin period, we constrained ourselves to the coadded spectra which includes 3 or more individual spectra with total exposure time of at least 45 minutes. With the possible exception of a few bright objects, the signal to noise of the individual spectra would not be sufficient to find indication for rotational changes. Therefore, we had to restrict ourself to simple models for the magnetic field geometry, namely centered magnetic dipoles with only two free parameters or to dipoles offset along the magnetic axis which have three free parameters. These parameters are the magnetic dipole field strength B_p , and the inclination of the dipole axis i for centered dipole. For the offset dipole there is an additional offset parameter along the magnetic axis z_{off} in terms of the stellar radius. For the 97 DAHs analyzed, we used the literature values for T_{eff} which were determined by comparison to the theoretical non-magnetic DA colors in the $u-g$ vs $g-r$ plane (Schmidt et al. 2003; Vanlandingham et al. 2005). The temperature of the new DAHs presented in Table 1 were estimated by the synthetic SDSS color-color diagrams by Holberg & Bergeron (2006)¹, assuming that the influence of the magnetic field at the temperature determination is small, which is not always the case (see Schmidt et al. 1986; Gänsicke et al. 2001, and Sec.4.2).

¹ <http://www.astro.umontreal.ca/~bergeron/CoolingModels/>

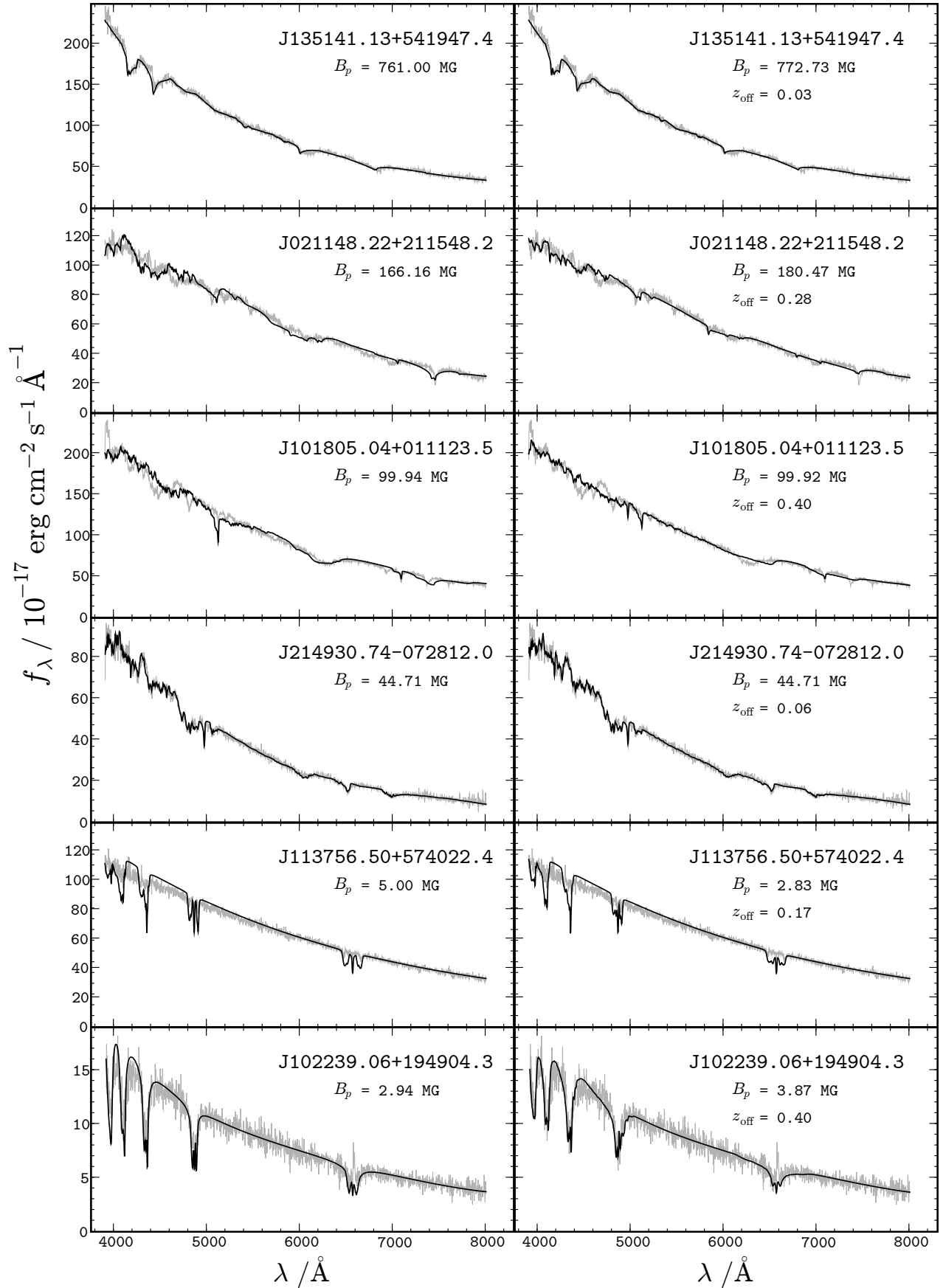


Fig. 1. Fits of observed spectra of DAHs from the SDSS to centered magnetic dipoles with a polar field strength B_p (left) and dipoles shifted by z_{off} stellar radii along the dipole axis (right). Representative fits and objects mentioned throughout the article are chosen. The color version of this figure and the remaining 128 fits can be found in the online version of this paper, [here](#).

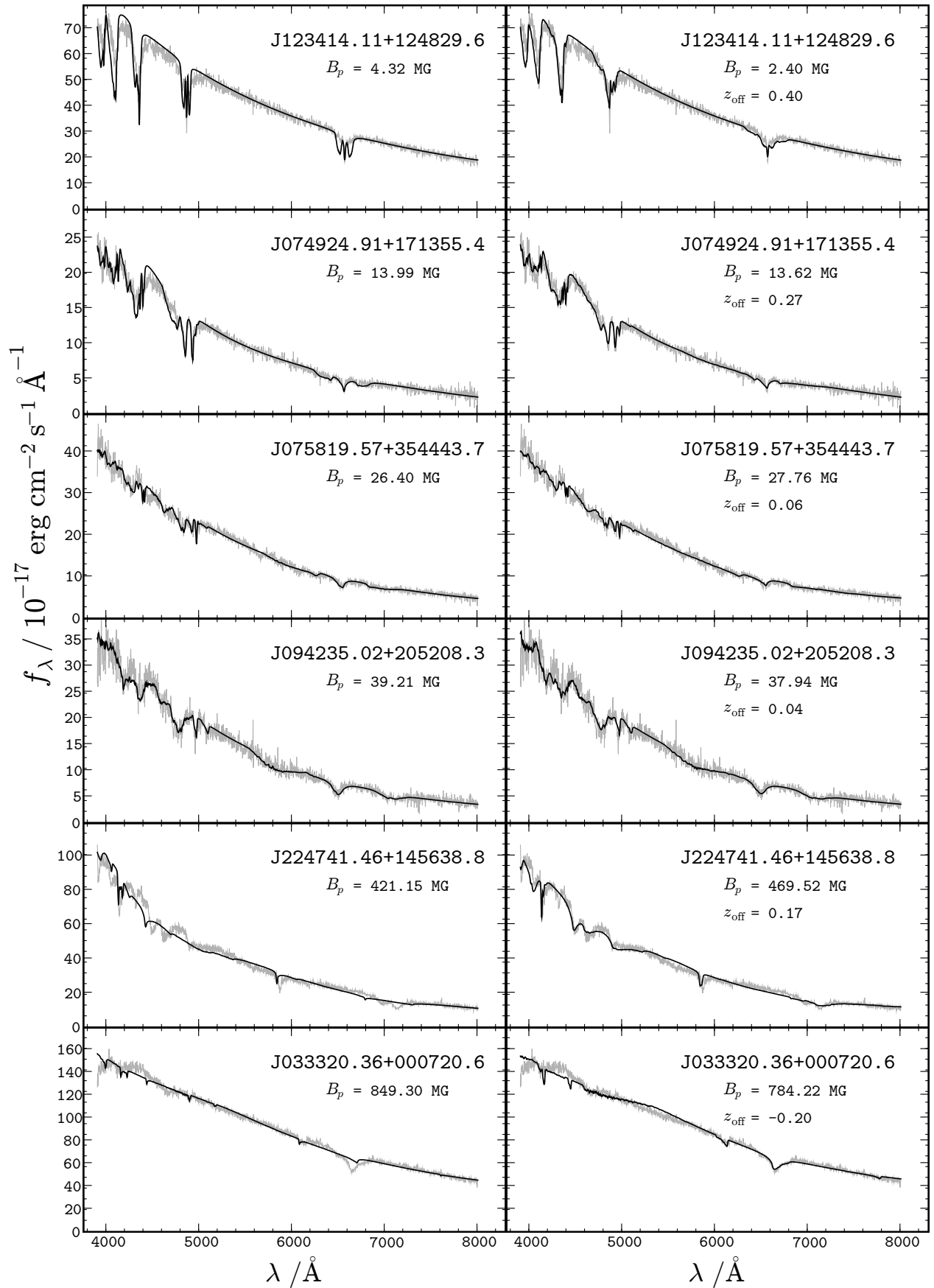


Fig. 2. Fits of observed spectra of DAHs from the SDSS to centered magnetic dipoles with a polar field strength B_p (left) and dipoles shifted by z_{off} stellar radii along the dipole axis (right). Representative fits and objects mentioned throughout the article are chosen. The color version of this figure and the remaining 128 fits can be found in the online version of this paper, [here](#).

Table 1. Photometric properties of the new confirmed DAHs and their temperatures. The columns indicate the SDSS name of the object; the plate, Modified Julian Date and fiber ids of the observations; the SDSS photometric magnitudes u , g , r , i , z ; and finally the temperatures derived from their colors.

MWD (SDSS+)	Plate-MJD-FiberID	u / mag	g / mag	r / mag	i / mag	z / mag	T_{eff} / K
J023420.63+264801.7	2399-53764-559	18.70	18.38	18.59	18.76	19.03	13500
J031824.19+422651.0	2417-53766-568	18.59	18.23	18.32	18.43	18.67	10500
J032628.17+052136.3	2339-53729-515	18.69	18.93	19.30	19.60	19.61	25000
J033320.36+000720.6	0415-51879-485	17.07	16.52	16.39	16.35	16.44	7000 ¹²
J074924.91+171355.4	2729-54419-282	18.78	18.78	19.13	19.44	19.64	20000
J075234.96+172525.0	1920-53314-106	18.78	18.44	18.44	18.50	18.64	9000
J080359.93+122943.9	2265-53674-033	17.24	17.23	17.53	17.83	18.08	9000
J081716.39+200834.8	2082-53358-444	18.91	18.34	18.15	18.12	18.23	7000
J083448.63+821059.1	2549-54523-135	18.07	18.32	18.74	19.06	19.49	27000
J083945.56+200015.7	2277-53705-484	18.11	17.83	18.11	18.36	18.66	15000
J085106.12+120157.8	2430-53815-229	17.35	16.96	17.14	17.30	17.56	11000
J085523.87+164059.0	2431-53818-522	18.78	18.55	18.80	19.05	19.32	15500
J085550.67+824905.3	2549-54523-066	18.40	18.60	18.91	19.23	19.46	25000
J091005.44+081512.2	1300-52973-639	17.38	17.54	17.96	18.28	18.65	25000
J091833.32+205536.9	2288-53699-547	18.73	18.41	18.66	18.92	19.22	14000
J093409.90+392759.3	1215-52725-241	18.72	18.35	18.40	18.50	18.55	10000
J094235.02+205208.3	2292-53713-019	18.41	18.42	18.80	19.05	19.26	20000
J100657.51+303338.1	1953-53358-415	19.22	18.83	18.90	19.04	19.18	10000
J100759.80+162349.6	2585-54097-030	18.01	17.70	17.80	17.96	18.19	11000
J101428.09+365724.3	52993-1426-021	19.26	18.87	18.97	19.09	19.43	10500
J102220.69+272539.8	2350-53765-543	20.47	20.05	20.16	20.38	20.69	11000
J102239.06+194904.3	2374-53765-544	19.43	19.01	19.01	19.11	19.13	9000
J103532.53+212603.5	2376-53770-534	17.98	17.40	17.23	17.19	17.21	7000 ²
J105709.81+041130.3	0580-52368-274	18.09	17.67	17.58	17.60	17.70	8000
J112030.34-115051.1	2874-54561-512	18.65	18.73	19.05	19.34	19.75	20000
J112257.10+322327.8	1979-53431-512	19.60	19.37	19.50	19.68	19.92	12500
J112328.49+095619.3	1222-52763-625	18.15	17.70	17.74	17.87	18.02	9500
J113215.38+280934.3	2219-53816-329	17.50	16.99	16.88	16.87	16.92	7000 ²
J124836.31+294231.2	2457-54180-112	18.44	17.80	17.59	17.54	17.56	7000 ²
J125434.65+371000.1	1989-53772-41	16.01	15.97	16.35	16.64	16.95	10000
J125715.54+341439.3	2006-53476-332	17.14	16.78	16.81	16.92	17.11	8500
J134820.79+381017.2	2014-53460-236	17.26	17.54	18.04	18.33	18.70	35000
J140716.66+495613.7	1671-53446-453	19.03	19.13	19.43	19.75	19.97	20000
J141906.19+254356.5	2131-53819-317	17.80	17.41	17.46	17.53	17.69	9000
J143019.05+281100.8	2134-53876-423	18.03	17.68	17.68	17.74	17.92	9000
J151130.17+422023.0	1291-52738-615	18.20	17.98	18.01	18.20	18.48	9500
J151415.65+074446.5	1817-53851-534	19.16	18.84	18.88	18.99	18.88	10000
J152401.60+185659.2	2794-54537-410	18.39	18.15	18.34	18.54	18.8	13500
J153843.10+084238.2	1725-54266-297	18.24	17.90	17.94	18.22	18.20	9500
J154305.67+343223.6	1402-52872-145	18.08	18.32	18.75	19.10	19.46	25000
J165249.09+333444.9	1175-52791-095	19.11	18.63	18.63	18.65	18.92	9000
J202501.10+131025.6	2257-53612-167	18.91	18.76	19.07	19.28	19.74	17000
J220435.05+001242.9	0372-52173-626	19.66	19.38	19.47	19.54	19.71	22000
J225726.05+075541.7	2310-53710-420	17.09	17.11	17.31	17.44	17.65	40000

¹ HE 0330-0002

² The temperature from fits to the color-color diagram is uncertain.

All fits have reduced χ^2 values between 0.8 and 3.0 except for some high-field objects which obviously deviate from the assumed dipole geometry (see Sect. 4). We use the error calculation method of Zhang et al. (1986), which assumes that a small change in χ^2 could be approximated by a linear expansion of the covariance matrix; for complex χ^2 topologies, this approximation is not sufficient. Moreover, the final error for the inclination is often very large.

Final fit parameters with errors are noted in Table 2. In Fig. 1 and 2 we have shown fits of 12 DAHs, as an example. All of our remaining resulting fitted spectra can be found in the online version of this article (Fig. A.3-A.23 for the other DAHs).

4. Results

4.1. Individual objects

Three objects analyzed by Schmidt et al. (2003) and Vanlandingham et al. (2005) are omitted in this work. *SDSSJ05959.56+433521.3* (*G111-49*) was listed by Schmidt et al. (2003) as a DAH, but is a Carbon-rich (DC) MWD (Putney 1995). *SDSSJ084716.21+148420.4* is a DAH+DB binary, in which the Helium component is quite strong in the spectrum. This dilution of the Hydrogen features hindered the analysis of this object by our code. Finally we failed to model *J220029.08-074121.5* due to the lack of any discernible features in the SDSS spectrum.

Emission lines were found in *SDSSJ102220.69+272539.8* and *SDSSJ102239.06+194904.3* (the latter is shown in Fig. 1),

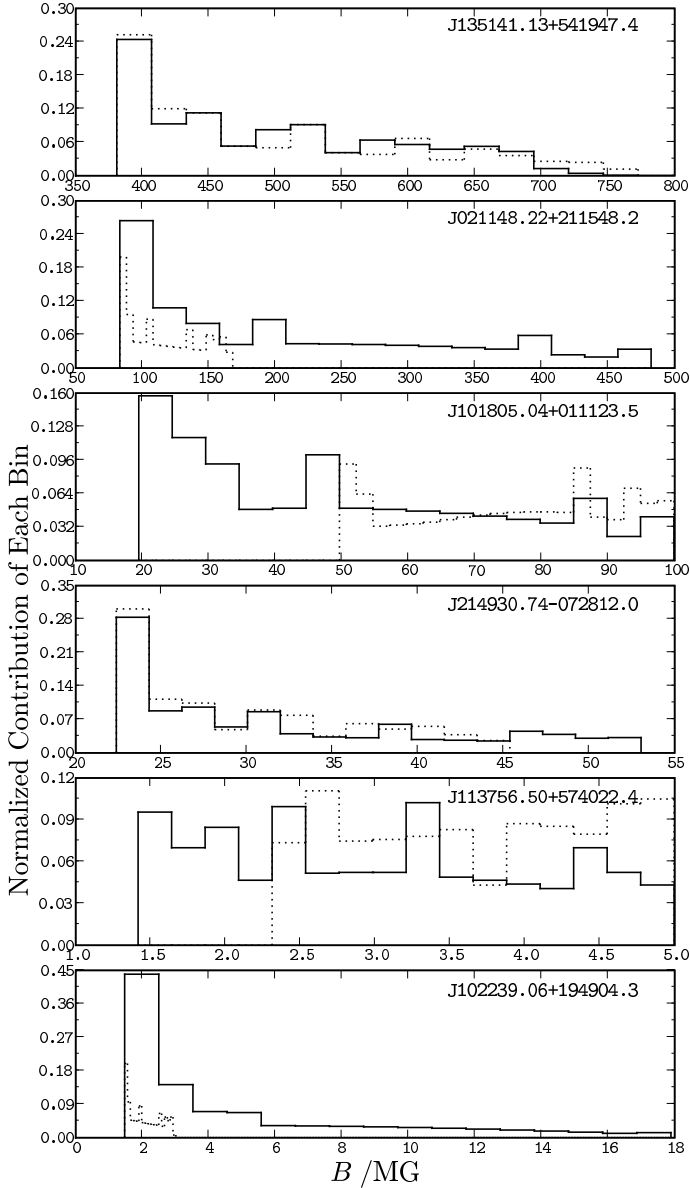


Fig. 3. Normalized histograms of the magnetic field strength distributions over the visible hemisphere of the star used for calculation of the synthetic spectra shown on Fig. 1. Dotted lines represent the centered dipole models, solid lines indicate dipole models with offsets.

very similar to *SDSSJ121209.31+013627.7* which could indicate that these objects may be EF Eri like, magnetic cataclysmic variables with a brown dwarf companion (Schmidt et al. 2005; Debes et al. 2006; Burleigh et al. 2006; Farihi et al. 2008).

The spectra of the high-field objects *SDSSJ224741.41+145638.8* and *SDSSJ101805.04+01123.5* (PG 1015+014, shown in Fig.1) do not fit particularly well. At higher field strengths (> 50 MG) the spectra become very sensitive to the details of the magnetic field geometry, as was demonstrated by Euchner et al. (2002, 2005, 2006). The deviations of the observed spectra from our theoretical spectra assuming (offset) dipole models hint therefore to a magnetic field geometry that is more complex than a shifted dipole. A more comprehensive analysis of *SDSSJ101805.04+01123.5* showed that individually tilted and off-centered zonal multipole components with field strengths between 50-90 MG is needed to represent the global

magnetic field (Euchner et al. 2006), which was consistent with our analysis.

The colors of MWDs with high field strengths (> 50 MG) are known to differ from non-magnetic white dwarf colors due to the absorption from their spectral features as noted in Sec.2. This behavior also affects temperature determinations from color-color diagrams. The analysis of *SDSSJ224741.41+145638.8* by Euchner et al. (2006) revealed effective temperature of $T_{\text{eff}} = 10000 \pm 1000$ K unlike $T_{\text{eff}} = 12000$ K that is derived from color-color diagrams. We have used 10000 K for our models and this value gave better results, especially on the basis of line depths. When color derived effective temperatures were used a similar discrepancy with the slopes and line depths was also observed in *SDSSJ224741.41+145638.8*. 17000 K was used in modeling by Schmidt et al. (2003), but the colors of *SDSSJ224741.41+145638.8* lies beyond the Holberg & Bergeron (2006) grid of $\log g - T_{\text{eff}}$ in $u-g-r$ plane. In our procedure we accomplished the best result with 50000 K for this object on the basis of slope and line depths. On the other hand, some high-field objects in our sample like *SDSSJ135141.13+541947* (Fig. 1) were fitted well and this discrepancy between the temperature derived by colors vs spectral fits was not observed.

For some fits, observed and computed spectra strongly differ in line depths. These unsatisfactory fits revealed two different kind of symptoms: Either σ^{\pm} components were shallower than expected from their sharp π counterparts in observed spectra with respect to the models; or both σ^{\pm} and π components of the lines were shallow at the same time.

The occurrence of sharp line cores with shallow wings in the spectra was already noted for *J123414.11+124829.6* by Vanlandingham et al. (2005). It has been suggested that this might be a result of deviation from centered dipole geometry, and our fits with offset dipole models proved to be considerably better than the centered dipole models in reduced χ^2 . For lower magnetic strengths (< 50 MG) the smearing effect of offset dipole models affects only the σ^{\pm} components of the lines. The reason is that in this field regime σ^{\pm} components become more separated while the π components are only slightly blue shifted with increasing field strength. Therefore smeared out wings with sharp line cores can be synthesized by adding up a larger range of magnetic field strength values. Dipole models with offsets can generate such extended magnetic field distributions (see Sec.4.2). Our fit to *J123414.11+124829.6* was considerably better but we did not reproduce the exact profile. Another possible explanation of such a spectrum is the contribution from a non-magnetic DA, which would dilute the σ^{\pm} components causing an increased contrast between wings and line cores. dipole models improved our fits, further analysis is needed to disentangle the effect of geometry versus possible contribution from a non-magnetic DA.

For the other case, *J113756.50+574022.4* (see Fig. 1) has very shallow features, with discernible magnetic wings. Neither a complicated geometry nor a change in effective temperature explains this lack of line depth. Nevertheless, the magnetic field strength could be derived from the extent of the wings. We suspect that this object may be an unresolved spectroscopic binary (e.g. with DA+DC components), since in these situations Hydrogen line strengths are known to be suppressed by the other component (Bergeron et al. 1990; Liebert et al. 1993). The other objects with shallow features which belong to this category are: *J084716.21+484220.4*, *J090632.66+080716.0*, *J113215.38+280934.3*, *J103532.53+212603.5*, *J112328.49+095619.3*, *J124806.38+410427.2*, *J141906.19+254356.5*.

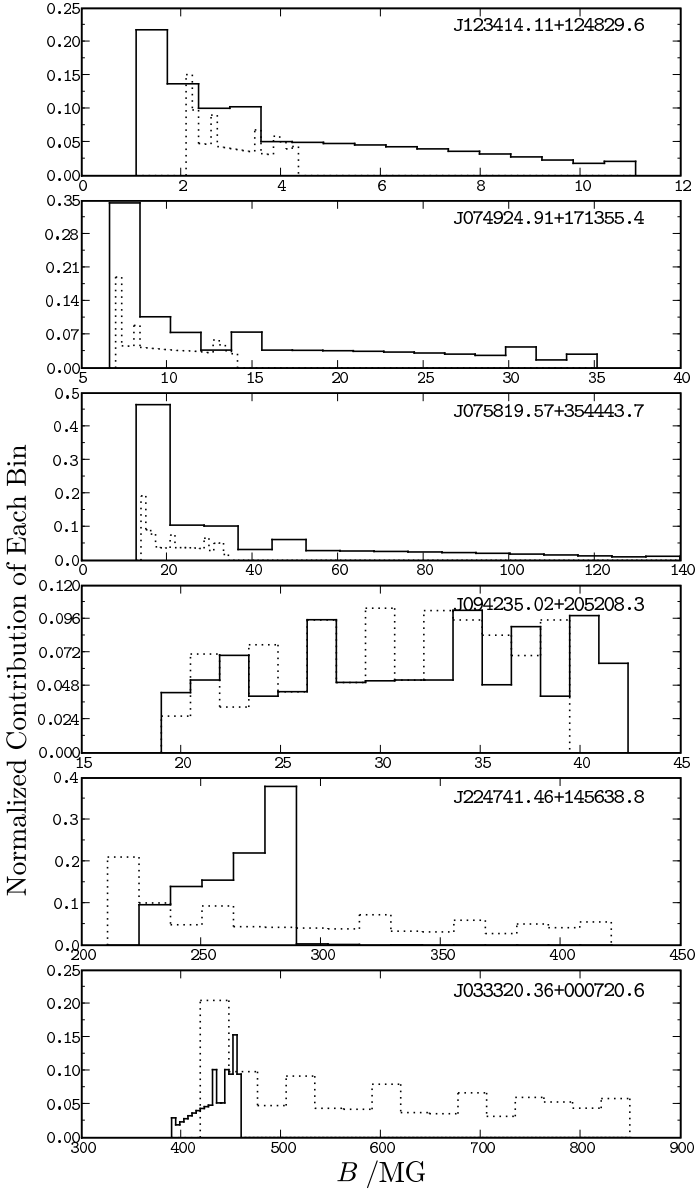


Fig. 4. Normalized histograms of the magnetic field strength distributions over the visible hemisphere of the star used for calculation of the synthetic spectra shown on Fig. 2. Dotted lines represent the centered dipole models, solid lines indicate dipole models with offsets.

One interesting outcome of our work was the modeling of *J033320.36+000720.6* which was formerly identified in the Hamburg/ESO survey for bright quasars, as HE 03330-0002 (Reimers et al. 1998). Its magnetic property was confirmed by Schmidt et al. (2001) by circular polarimetry; nevertheless the modeling of the HE 03330-0002 was not possible, since the transitions in its spectrum were thought not to be explainable with hydrogen or with helium transitions. Although *J033320.36+000720.6* was already discovered in the EDR, due to this lack of knowledge about the atmosphere Gänsicke et al. (2002) did not try to model it with pure hydrogen atmosphere.

However we have noticed that some of the lines in the spectrum of *J033320.36+000720.6* possibly coincided with hydrogen stationary lines. With this incentive we modeled it with a 7000 K DAH atmosphere. Our initial fits with a centered dipole resulted in a dipolar field strength of ~ 850 MG (see Fig 2)

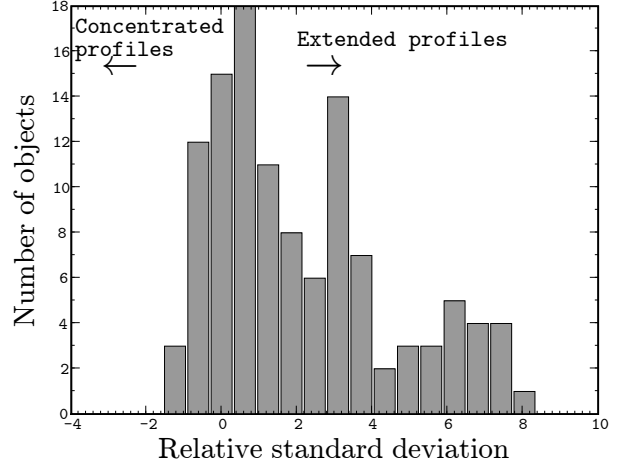


Fig. 5. Histogram of the relative variance σ_{rel} (see Sec. 4.2) for known SDSS MWDs. Negative σ_{rel} indicates a magnetic field strength profile of the visible surface which is more concentrated than a centered dipole, whereas positive indicates profiles that are more extended.

Table 2. The hydrogen transitions of SDSSJ033320.36+000720.6 and their wavelengths at 446.5 MG.

Line	$n l m - n' l' m'$	$\lambda(\text{\AA})$
H α	$2s_0 - 3p_0$	6113.05
H α	$2s_0 - 3p_{-1}$	7710.91
H α	$2p_{-1} - 3d_{-2}$	6647.76

which produced the position but not the depths of three transitions. More careful modeling with an offset dipole showed that the mean field strength over the visible surface is much more concentrated than a regular dipole field geometry. Fig. 4 shows that the mean field strength is dominated by an interval of field strengths between 390 – 470 MG. When we consider the apparent peak value of this distribution, we get commensurable line positions for three lines in the spectrum as H α transitions (see table 2).

The pure hydrogen atmosphere did not account for the red part ($\lambda < 5500\text{\AA}$) of the spectrum. Apparently there are additional opacity contributions from different species of elements, both to continuum and to the line features.

4.2. Magnetic field geometry

In this work we have modeled a large sample of DAHs with dipole magnetic fields with offsets of the magnetic axis. However, visualization of these model parameters is not straightforward. The effect of the dipole offset on the model spectrum depends on both inclination and the polar field strength. However, the polar field strength is not a representative value for the global magnetic field on the visible surface if the offsets are large. The most direct way to investigate a model geometry is to construct a diagram with the angle between the line of sight and the local magnetic field vector versus the magnetic field strength plots which are equivalent to the Zeeman Broadening Analysis (ZEBRA) plots of (Donati et al. 1994). For our case since we did not have polarization data, we only considered the magnetic field strength distribution histograms for simplicity.

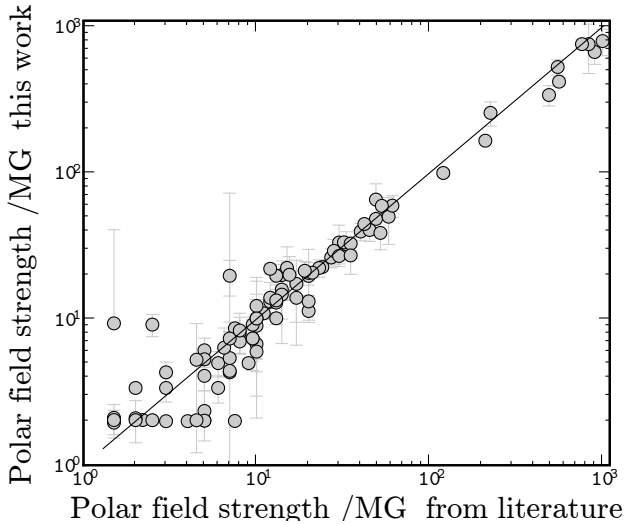


Fig. 6. Comparison of centered dipole magnetic field fit values in this work versus Schmidt et al. (2003), Vanlandingham et al. (2005).

In general the effect of the offset dipole models is to extend or reduce the range of magnetic field strengths over the visible surface of the MWD, which is a fixed factor of two for centered dipole models (see Fig. 3). For offset dipoles the range depends on the values of B_p and the inclination i . In order to quantify the difference between the centered and off-centered dipole models we determined the average and the standard deviation σ of the distribution of the magnetic fields for the parameters of our best fits. The relative change of the standard deviations σ_{centered} and σ_{offset} is given by $\sigma_{\text{rel}} = \frac{\sigma_{\text{offset}} - \sigma_{\text{centered}}}{\sigma_{\text{centered}}}$.

$\sigma_{\text{rel}} = 0$ indicates that the width of the centered and offset dipole models are the same; $\sigma_{\text{rel}} < 0$ means more concentrated than a dipole field, in the case of $\sigma_{\text{rel}} > 0$ the distribution of field strengths is more extended.

To discuss the magnetic field geometry of our sample, we plotted the histogram of σ_{rel} values for all known SDSS DAHs except the ones that were discussed in Sec. 4.1 as possible binaries (Fig. 5). The average σ_{rel} for this sample turned out to be 2.18. This means even with rather mediocre signal to noise spectra of SDSS, an overall the tendency towards non-dipolarity is observed in our sample of white dwarfs.

4.3. General discussion

Overall our results are consistent with the former analyses on DAHs (see Fig. 6), which shows that simple atmosphere models with pre-assumed dipole magnetic values are good approximations for these objects. In all of the cases offset dipole models resulted in significantly better fits than the models with centered dipoles. We have noted in Section 4.1 that still for some DAHs with high fields, completely satisfactory fits cannot be achieved with offset dipole models. This hints to a magnetic field geometry that is more complex than a shifted dipole.

The dipole magnetic field Ohmic decay timescale is 10^{10} yr. Even the higher multipoles can live for such a long period of time (Muslimov et al. 1995). Therefore, no significant correlation between temperature and magnetic field strength is expected if temperature is assumed as an indicator of age (Fig. 8). This

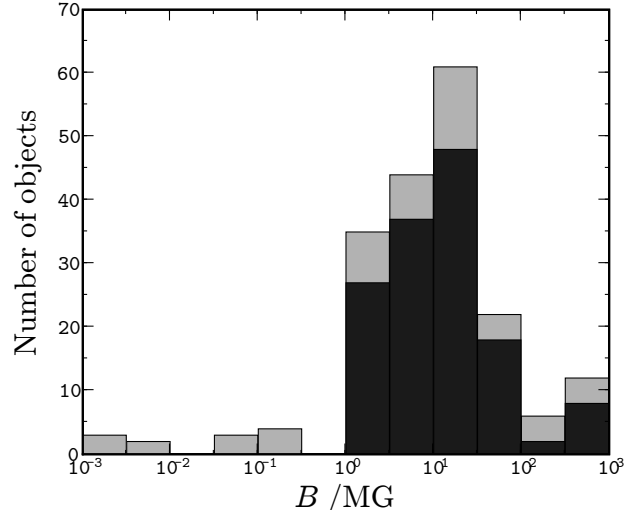


Fig. 7. Histogram of the known magnetic white dwarfs in equal intervals of $\log B$. Gray columns represent the number of all known DAHs. Black shades represent the the contribution of SDSS to DAHs.

lack of correlation supports the fossil ancestry of these fields inherited from earlier stages of stellar evolution.

5. Conclusion

In this paper we have analysed 141 DAHs, 97 of them previously analysed and 44 of them being new. Gänsicke et al. (2002) conservatively estimated that the total number of MWDs would be tripled by the complete SDSS coverage. This expectation is already surpassed before the end of the systematic search over the latest data releases. Additionally our consistent modeling over the data releases, show that within the SDSS DAH population there is a tendency to deviate from simple centered dipoles. There are clear indications of deviation from centered dipole models in least 50% of the SDSS DAHs (see Fig 5).

The distribution of the magnetic field strengths of the MWDs from the Schmidt et al. (2003) sample is concentrated in the $\sim 5 - 30$ MG interval. We have updated the magnetic field strengths of all known DAHs and created a histogram (Fig. 7). The values were taken from Jordan (2009), which is an extended and corrected version of Kawka et al. (2007). The same overabundance in the range $\sim 5 - 30$ MG as discussed in Schmidt et al. (2003) is apparent in Fig. 7, but overall SDSS has nearly tripled the number of DAHs and conversely the completeness of the total MWD population is affected significantly by the SDSS biases because of this high impact of SDSS.

High field MWDs are thought to be remnants of magnetic Ap and Bp stars. If flux conservation is assumed, the distribution of the polar field strengths of high field MWDs should be largest in the interval 50–500 MG. In our sample, objects with magnetic field strengths lower than 50 MG are more numerous than the objects with higher magnetic field strengths (see Fig. 7). Part of this effect is due to our biases (see Section 2). Nevertheless it is consistent with previous results and supports the hypothesis that magnetic fossil fields from Ap/Bp stars only are not sufficient to produce high field MWDs (Wickramasinghe & Ferrario 2005). Aurière et al. (2007) argued that dipole magnetic field strengths of magnetic Ap/Bp stars have a “magnetic threshold” due to

large scale stability conditions, and this results in a steep decrease in the number of magnetic Ap/Bp stars below polar magnetic fields of 300 G.

A possible progenitor population for MWDs with dipolar field strengths below 50 MG is the currently unobserved population of A and B stars with magnetic field strengths of 10–100 G. Wickramasinghe & Ferrario (2005) suggested that if $\sim 40\%$ of A/B stars have magnetism, this would be sufficient to explain the observed distribution of MWDs. However, the existence of this population seems to be highly unlikely since investigations of Shorlin et al. (2002) and Bagnulo et al. (2006) for magnetism in this population yielded null results, for median errors of 15–50 G and 80 G, respectively. Another candidate group for these MWDs with lower field strengths is the yet undetected magnetic F stars (Schmidt et al. 2003). But this conclusion is strongly affected by SDSS MWD discovery biases.

In our work we quantified the deviation from centered dipoles in our sample. To test the fossil field hypothesis one can look at the statistical properties of the fields of Ap/Bp stars. One such statistical analysis was made by Bagnulo et al. (2002). In their work they used the mean longitudinal field, the crossover, the mean quadratic field and the mean field modulus to invert the magnetic field structure modeled by a dipole plus quadrupole geometry (the modeling procedure is explained in depth in Bagnulo et al. 1996; Landolfi et al. 1998). The aim of this analysis was to characterize the sample rather than find the best fit for each object. Using the aforementioned observables they analyzed 31 objects and ended up with 147 “good fit” models. These models corresponded to the minima of the χ^2 hypersurfaces in their inversion procedure. Later model parameters were weighted by these reduced χ^2 values in assessing their statistical properties.

Bagnulo et al. (2002) investigated the quadrupole vs dipole dominance of the magnetic field models by plotting weighted histograms of B_d/B_q . Where B_d is amplitude of dipole field strength (B_p in this work), and B_q is the amplitude of the quadrupole field strength. The main differences between our analysis and Bagnulo et al. (2002) was the usage of visual magnetic field distributions rather than the global magnetic field inferred from the time resolved observations. The relationship between B_d/B_q to our skew parameter is not so straightforward since the structure of the total field depends on the angle between dipole and quadrupole components. If we were to consider $B_d/B_q = 1$ as the point where quadrupole component starts to dominate, 63% of the models can be considered dominantly quadrupolar (see Fig. 3 of Bagnulo et al. 2002). Hence our conservative assessment of at least 50% of DAHs having non dipolar field, seems to be consistent with this result.

However one needs to be careful in considering the correspondence between the geometry between MWDs and their progenitors since theoretical models expect the field on the surface to evolve under certain conditions. Braithwaite & Spruit (2004) investigated the stable configurations of magnetic fields in stars with their magnetohydrodynamics code. Their work resolves that initial random fields decay and within a few Alfvén timescales to a poloidal plus toroidal stable configuration. During the star’s evolution, its toroidal field may diffuse outwards since the Ohmic diffusion time scale is within the order of the lifespan of an Ap/Bp star (Braithwaite & Nordlund 2006). On the Ohmic time scale, the expected initial offset-dipole configuration of the surface magnetic field evolves to a simple centered dipole. Hence Braithwaite & Nordlund (2006) hypothesized that Ap stars with centered dipole fields are likely to be older than Ap stars with non-dipolar geometries. It is important

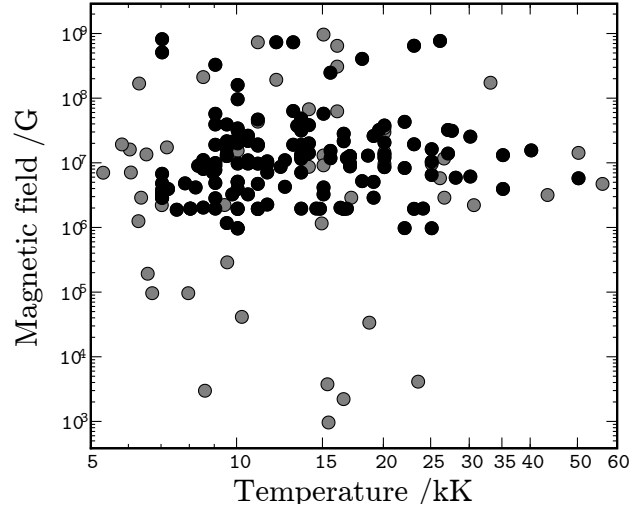


Fig. 8. Scatter plot of dipole magnetic field value vs temperature. While black dots represent all known SDSS DAHs, grey dots indicate the DAHs from literature that were not analyzed in this work. The random distribution of field strengths with respect to age indicator temperature is consistent with long decay timescale of DAHs with respect to their cooling age.

to mention that the concentration of the field inside the star is also an important parameter which contributes to the structure of the surface magnetic field. A highly concentrated field results in a surface field structure with higher order multiples after the internal toroidal field formation. The relative importance between the Ohmic diffusion (i.e. the age) and concentration of the initial field on the surface magnetic field structure was not further investigated. Nevertheless if the Ohmic diffusion timescale is effective in the lifetime of an Ap star, then the field configurations of an older population of Ap stars are more relevant for comparison to the magnetic field distribution of MWDs. This kind of work has not been undertaken for the Ap stars yet.

If we neglect the possibility that older Ap stars may behave differently from the whole sample of this group and the field structure of MWDs do not evolve unlike what Muslimov et al. (1995) suggested (see Sec. 4.3, then the global analysis of Bagnulo et al. (2002) implicates that the distribution of field structures of chemically peculiar stars and DAHs are comparable, hence supporting the fossil field hypothesis.

In addition to the isolated evolution scenario, recently a binary star origin was proposed by Tout et al. (2008) for generating magnetic fields in WDs. In this picture during the evolution to the cataclysmic variables (CVs) the cores of giants go to a common envelope (CE) phase. During this phase the orbital angular momentum is transferred to the envelope as the two cores spiral in together. This process causes differential rotation and convection within the CE, which are the ingredients for magnetic field generation (see Tout et al. 2008, and references therein).

A consistent account for the origins of magnetic fields in WDs awaits the finalization of the complete sample of SDSS MWDs.

Table 2. Model fits with centered dipole and offset dipole models with comparison to literature values. The columns indicate the SDSS name of the object; the plate, Modified Julian Date and fiber ids of the observations; the dipole magnetic field strength of the centered dipole, the inclination with respect to the line of sight of the centered dipole, the dipole magnetic field strength of the offset dipole, the inclination with respect to the line of sight of the offset dipole, the offset along the axis of the magnetic field in terms of the stellar radius, and finally comments indicate the model parameters from the literature (i.e. Gänsicke et al. 2002; Schmidt et al. 2003; Vanlandingham et al. 2005)

MWD (SDSS+)	Plate-MJD-FiberID	B_p / MG	i / deg	B_{off} / MG	$z_{\text{off}} / r_{\text{WD}}$	i / deg	fits
J002129.00+150223.7	753-52233-432	530.69±63.56	53.19 ± 25.64	527.33±97.98	0.16±0.08	28.05 ± 51.8	550 MG, ...
J004248.19+001955.3	690-52261-594	2.00 ± 0.00 ²	88.22 ± 43.37	2.58 ¹	0.35±0.82	0.00 ± 23.66	14 MG, 30°
J021116.34+003128.5	405-51816-382	341.31±54.34	37.73 ± 27.71	281.34±186.95	0.32±0.14	9.59 ± 62.99	490 MG, ...
J021148.22+211548.2	246-53327-048	166.16 ± 7.41	48.89 ± 5.67	180.47 ± 13.15	0.27 ± 0.02	33.23 ± 10.05	210 MG, 90°
J023420.63+264801.7	2399-53764-559	32.82 ± 6.26	42.08 ± 8.09	21.17 ± 2.02	0.38 ± 0.04	17.17 ± 10.92	
J030407.40-002541.7	411-51817-172	10.95±0.98	48.57 ± 5.72	11.13±0.97	0.27±0.10	51.51 ± 17.26	11 MG, 60°
J031824.19+422651.0	2417-53766-568	10.12±0.10	54.6 ± 4.7	10.77±0.10	0.29±0.05	61.1 ± 10.0	
J032628.17+052136.3	2339-53729-515	16.87 ± 2.41	53.06 ± 26.65	17.49 ± 8.32	0.34 ± 0.12	44.62 ± 42.63	
J033145.69+004517.0	415-51879-378	13.13±1.00	49.41 ± 38.17	12.12±9.98	0.21±0.02	47.43 ± 38.49	12 MG, 60°
J033320.36+000720.6	0415-51879-485	849.30 ± 51.75	50.92 ± 8.75	784.22 ± 83.98	0.19 ± 0.05	6.29 ± 6.42	
J034308.18-064127.3	462-51909-117	9.96±2.06	41.96 ± 9.80	9.18±2.11	0.23±0.04	12.59 ± 8.55	13 MG, 45
J034511.11+003444.3	416-51811-590	1.96±0.42	49.01 ± 11.56	1.46±0.36	0.34±0.08	16.38 ± 6.43	1.5 MG, 0°
J074850.48+301944.8	889-52663-507	6.75±0.41	40.65 ± 7.59	8.03±0.66	0.40±0.14	43.85 ± 10.55	10 MG, 60°
J074924.91+171355.4	2729-54419-282	13.99 ± 1.30	46.00 ± 15.07	13.62 ± 1.86	0.27 ± 0.05	44.02 ± 53.16	
J075234.96+172525.0	1920-53314-106	10.30±1.23	72.4 ± 22.4	11.73±1.05	0.26±0.05	58.7 ± 38.1	
J075819.57+354443.7	757-52238-144	26.40±3.94	37.62 ± 22.98	32.42±5.65	0.39±0.07	54.51 ± 19.44	27 MG, 30°
J080359.93+122944.0	2265-53674-033	40.7 ± 2.13	42.97 ± 8.44	26.6 ± 11.8	0.26±0.04	17.71 ± 7.21	
J080440.35+182731.0	2081-53357-442	48.47±2.93	35.67 ± 7.59	29.26±3.18	0.16±0.02	33.97 ± 8.47	49 MG, 30°
J080502.29+215320.5	1584-52943-132	6.11±1.29	54.76 ± 14.52	3.13±0.59	0.39±0.06	86.79 ± 59.37	5 MG, 60°
J080743.33+393829.2	545-52202-009	65.75±18.52	78.07 ± 35.46	64.74±12.14	-0.01±0.01	8.25 ± 17.26	49 MG, 30°
J080938.10+373053.8	758-52253-044	39.74±5.41	41.89 ± 14.11	30.60±5.66	0.20±0.10	15.15 ± 75.23	40 MG, 30°
J081648.71+041223.5	1184-52641-329	10.13±8.03	48.82 ± 29.96	6.50±2.73	0.31±0.12	0.28 ± 27.06	10* MG, 30*°
J081716.39+200834.8	2082-53358-444	3.37 ± 0.44	49.02 ± 10.78	3.37 ± 1.09	0.39±0.10	34.05 ± 30.78	
J082835.82+293448.7	1207-52672-635	33.40±10.53	68.57 ± 33.47	34.60±6.91	0.17±0.05	50.3 ± 36.21	30 MG, 90*°
J083448.63+821059.1	2549 54523 135	14.44 ± 4.57	54.30 ± 66.45	14.36 ± 4.08	0.28 ± 0.09	48.58 ± 70.00	
J083945.56+200015.7	2277-53705-484	3.38±0.49	48.6 ± 7.7	2.15±0.10	0.29±0.08	49.9 ± 90 ¹	
J084155.74+022350.6	564-52224-248	5.00±0.99	49.35 ± 17.53	2.94±0.72	0.16±0.04	15.89 ± 10.57	6 MG, 90°
J085106.12+120157.8	2430-53815-229	2.03±0.10	81.9 ± 90 ¹	2.47±0.10	0.35±0.06	72.8 ± 18.8	
J085523.87+164059.0	2431-53818-522	12.23±2.92	48.6 ± 8.6	7.86±1.63	0.36±0.06	10.8 ± 6.1	
J085550.67+824905.3	2549 54523 066	10.82 ± 2.99	54.81 ± 19.36	12.13 ± 4.30	62.89 ± 36.38	0.30 ± 0.14	
J085830.85+412635.1	830-52293-070	3.38±0.19	48.85 ± 5.86	2.15±0.34	0.24±0.07	36.25 ± 7.31	2 MG, 30°
J090632.66+080716.0	1300-52973-148	5.98 ± 3.02	88.00 ± 88.06	5.97 ± 3.13	0.18 ± 0.13	65.13 ± 82.65	10 MG, 90°
J090746.84+353821.5	1212-52703-187	22.40±8.80	48.57 ± 16.68	11.91±3.22	0.26±0.08	1.77 ± 2.72	15 MG, 60°
J091005.44+081512.2	1300-52973-639	1.01 ± 0.00 ²	74.46 ± 42.54	1.27 ± 0.70	71.06 ± 32.03	0.35 ± 0.29	
J091124.68+420255.9	1200-52668-538	35.20±5.83	35.1 ± 39.48	18.85±4.86	0.23±0.06	14.23 ± 10.72	45 MG, 60°
J091437.40+054453.3	1193-52652-481	9.16±0.77	48.52 ± 4.56	8.93±0.93	0.38±0.04	48.35 ± 19.7	9.5 MG, 90°
J091833.32+205536.9	2288-53699-547	2.04±0.10	87.2 ± 41.9	2.66±1.71	0.39±0.17	70.3 ± 61.9	
J092527.47+011328.7	475-51965-315	2.04 ± 0.00 ²	54.83 ± 14.14	3.14±1.10	0.33±0.13	47.34 ± 14.08	2.2 MG, ...
J093356.40+102215.7	1303-53050-525	2.11±0.49	72.05 ± 22.68	2.47 ± 0.00 ²	0.37±0.12	52.39 ± 29.38	1.5 MG, 60*°
J093409.90+392759.3	1215-52725-241	1.01 ± 0.00 ²	81.18 ± 23.30	1.35 ± 0.25	57.43 ± 29.65	0.39±0.13	
J093447.90+503312.2	901-52641-373	7.35±2.21	54.61 ± 37.93	4.29±1.06	0.28±0.07	46.87 ± 49.83	9.5 MG, 60°

Table 2. continued.

MWD (SDSS+)	Plate-MJD-FiberID	B_p / MG	i / deg	B_{off} / MG	$z_{\text{off}} / r_{\text{WD}}$	i / deg	Comments
J094235.02+205208.3	2292-53713-019	39.21 ± 4.55	3.73 ± 1.64	37.94 ± 9.07	0.04 ± 0.02	1.24 ± 13.74	
J094458.92+453901.2	1202-52672-577	15.91±9.10	68.35 ± 44.53	17.41±7.12	0.34±0.14	61.00 ± 90 ¹	14 MG, 90°
J100005.67+015859.2	500-51994-557	19.74±10.26	48.5 ± 33.13	8.10±3.23	0.34±0.13	4.21 ± 90 ¹	20 MG, 30°
J100356.32+053825.6	996-52641-295	672.07±118.63	40.8 ± 34.86	667.67±131.71	0.08±0.05	36.67 ± 23.11	900* MG, ...
J100657.51+303338.1	1953-53358-415	1.00±0.10	82.5 ± 30.8	1.30±1.23	-0.37±0.39	14.3 ± 13.1	
J100715.55+123709.5	1745-53061-313	5.41±67.28	68.6 ± 31.88	6.01±2.55	0.40±0.22	50.7 ± 90 ¹	7 MG, 60°
J100759.80+162349.6	2585 54097 030	19.18 ± 3.36	42.02 ± 17.48	13.50 ± 2.92	-0.22 ± 0.05	33.31 ± 21.38	
J101428.09+365724.3	1954-53357-393	11.09 ± 1.50	48.75 ± 11.72	12.14 ± 2.71	0.05 ± 0.04	56.81 ± 34.40	
J101529.62+090703.8	1237-52762-533	4.09±0.86	49 ± 15.27	1.98±0.35	0.26±0.08	1.48 ± 60.69	5* MG, 90*°
J101618.37+040920.6	574-52355-166	2.01 ± 0.00 ²	88.16 ± 104.01	7.24±4.77	0.19±0.16	60.55 ± 63.4	7.5 MG, 30°
J101805.04+011123.5	503-51999-244	99.92 ± 5.90	27.24 ± 6.16	39.87±2.25	0.26 ± 0.02	14.85 ± 3.17	120 MG, ...
J102220.69+272539.8	2350-53765-543	4.91 ± 0.31	27.58 ± 30.65	5.79 ± 2.82	0.39 ± 0.27	54.97 ± 35.63	
J102239.06+194904.3	2374-53765-544	2.94±0.71	49.0 ± 13.0	3.87±1.11	0.40±0.07	51.3 ± 40.3	
J103532.53+212603.5	2376-53770-534	2.96 ± 0.33	49.01 ± 9.51	1.515 ± 0.313	0.39 ± 0.05	0.00 ± 57.44	
J105404.38+593333.3	561-52295-008	17.41±7.90	90.0 ± 25.54	17.60±10.22	0.16 ± 0.05	67.59±59.48	17 MG, 90°
J105628.49+652313.5	490-51929-205	29.27±5.78	41.74 ± 15.24	20.80±4.10	0.29±0.54	5.27 ± 12.8	28 MG, 60°
J105709.81+041130.3	580-52368-274	2.03 ± 0.00 ²	48.99 ± 7.70	2.48 ± 0.0	41.40 ± 13.13	0.38 ± 0.06	
J111010.50+600141.4	950-52378-568	6.37±2.32	68.6 ± 16.26	6.71±1.58	0.39±0.08	49.08 ± 18.99	6.5 MG, 70°
J111812.67+095241.3	1222-52763-477	3.38±0.72	48.14 ± 32.44	2.67±0.60	0.40±0.10	51.09 ± 43.5	6 MG, 60*°
J112030.34-115051.1	2874-54561-512	8.90 ± 1.02	50.37 ± 20.24	7.72 ± 1.24	0.35 ± 0.10	38.69 ± 34.08	
J112257.10+322327.8	1979-53431-512	11.38±3.42	49.0 ± 12.3	7.46±1.68	0.37±0.11	4.2 ± 6.3	
J112328.49+095619.3	1222-52763-625	1.21 ± ²	81.18 ± 17.28	1.50 ± 0.36	0.39 ± 0.06	50.93 ± 90 ¹	
J112852.88-010540.8	326-52375-565	2.00 ± 0.00 ²	89.4 ± 85.15	2.30±5.02	0.20±0.14	23.15 ± 30.18	3 MG, 60°
J112926.23+493931.8	966-52642-474	5.31±0.64	48.72 ± 6.34	2.43±0.33	0.39±0.09	7.04 ± 12.45	5 MG, 60°
J113215.38+280934.3	2219-53816-329	3.01 ± 0.82	49.00 ± 17.43	2.84 ± 0.43	0.39 ± 0.049	18.60 ± 5.56	
J113357.66+515204.8	879-52365-586	8.64±0.78	74.55 ± 19.87	7.69±0.69	0.39±0.04	47.91 ± 19.99	7.5 MG, 90°
J113756.50+574022.4	1311-52765-421	5.00±0.34	33.45 ± 9.92	2.83±0.25	0.17±0.01	0.07 ± 0.06	9 MG, 60*°
J113839.51-014903.0	327-52294-583	22.71±1.26	54.31 ± 14.41	24.09±1.92	0.21±0.04	50.16 ± 61.4	24 MG, 60°
J114006.37+611008.2	776-52319-042	50.19±17.78	21.8 ± 42.46	52.82±8.82	0.04±0.02	36.88 ± 50.59	58 MG, 20°
J114829.00+482731.2	1446-53080-324	32.47±7.11	80.89 ± 45.93	32.44±2.70	0.17±0.09	69.98 ± 33.06	33 MG, 90°
J115418.14+011711.4	515-52051-126	33.47±2.07	88.14 ± 23.62	25.72±2.51	0.10±0.03	76.03 ± 32.13	32 MG, 45
J115917.39+613914.3	777-52320-69	20.10±6.70	50.63 ± 62.9	10.14±6.89	0.30±0.07	50.63 ± 62.9	15.5 MG, 60°
J120150.10+614257.0	778-52337-264	11.35±1.53	28.04 ± 10.98	7.60±0.87	0.16±0.02	18.59 ± 12.62	20 MG, 90°
J120609.80+081323.7	1623-53089-573	760.63±281.66	30.74 ± 36.38	312.24±73.90	0.24±0.13	25.69 ± 24.66	830* MG, ...
J120728.96+440731.6	1369-53089-048	2.03 ± 0.00 ²	73.01 ± 29.93	2.07 ± 0.00 ²	-0.27±0.59	10.16 ± 21.53	2.5 MG, 90°
J121209.31+013627.7	518-52282-285	10.12±0.93	48.8 ± 4.69	10.38±1.02	0.29±0.05	40.65 ± 13.27	13 MG, 80°
J121635.37-002656.2	288-52000-276	59.70±10.23	37.85 ± 37.52	44.57±7.18	-0.06±0.01	20.15 ± 30.89	61 MG, 90°
J122209.44+001534.0	289-51990-349	14.70±4.70	82.52 ± 90 ¹	16.27±11.39	0.24±0.31	82.52 ± 90 ¹	14 MG, 80°
J122249.14+481133.1	1451-53117-582	8.05±2.24	56.67 ± 13.05	8.70±3.90	-0.38±0.08	53.05 ± 18.28	8 MG, 90*°
J122401.48+415551.9	1452-53112-181	22.36±3.02	66.08 ± 23.71	24.75±5.76	0.26±0.06	58.28 ± 23.89	23* MG, 60°
J123414.11+124829.6	1616-53169-423	4.32±0.27	49.35 ± 9.82	2.40±0.56	0.40±0.05	9.99 ± 2.72	7 MG, 60*°
J124806.38+410427.2	1456-53115-190	7.03±1.19	48.81 ± 9.27	3.61±0.47	0.29±0.06	5.5 ± 10.08	8 MG, 90°
J124836.31+294231.2	2457-54180-112	3.95 ± 0.25	48.93 ± 4.93	-	-	-	
J124851.31-022924.7	337-51997-264	7.36±2.19	48.9 ± 10.11	8.01±1.46	0.40±0.09	49.97 ± 27.39	7 MG, 40°

Table 2. continued.

MWD (SDSS+)	Plate-MJD-FiberID	B_p / MG	i / deg	B_{off} / MG	$z_{\text{off}} / r_{\text{WD}}$	i / deg	Comments
J125044.42+154957.4	1770-53171-530	20.71±3.66	56.7 ± 11.21	20.30±2.43	0.12±0.02	53.83 ± 38.18	20 MG, 60°
J125416.01+561204.7	1318-52781-299	38.86±9.03	20.97 ± 40.41	36.98±9.20	0.01 ± 1e + 99	10.25 ± 21.24	52 MG, 30°
J125434.65+371000.1	1989-53772-041	4.10±0.35	41.9 ± 19.2	4.89±0.42	0.40±0.03	50.1 ± 21.0	
J125715.54+341439.3	2006-53476-332	11.45±0.71	0.5 ± 0.6	13.70±1.69	0.07±0.02	7.7 ± 12.0	
J132002.48+131901.6	1773-53112-011	2.02 ± 0.00 ²	88.21 ± 80.46	2.64±4.88	-0.38±0.52	6.99 ± 35.73	5 MG, 60°
J133340.34+640627.4	603-52056-112	10.71±1.03	50.29 ± 11.45	13.81±1.36	0.38±0.07	55.7 ± 24.63	13 MG, 60°
J134043.10+654349.2	497-51989-182	4.32±0.76	49.04 ± 9.75	5.28±1.07	0.40±0.06	34.03 ± 6.8	3 MG, 60°
J134820.79+381017.2	2014-53460-236	13.65±2.66	89.4 ± 90 ¹	14.45±4.65	0.22±0.04	54.8 ± 25.3	
J135141.13+541947.4	1323-52797-293	761.00±56.42	74.18 ± 21.65	772.73±94.41	-0.03±0.01	68.25 ± 62.04	760 MG, 20°
J140716.66+495613.7	1671-53446-453	12.49±6.20	88.1 ± 90 ¹	13.20±4.21	0.24±0.10	63.3 ± 81.1	
J141906.19+254356.5	2131-53819-317	2.03±0.10	81.2 ± 8.7	2.56±0.10	0.38±0.03	54.8 ± 10.4	
J142703.40+372110.5	1381-53089-182	27.04±3.20	56.89 ± 12.61	30.59±2.34	0.20±0.02	6.39 ± 22.5	30 MG, 60*°
J143019.05+281100.8	2134-53876-423	9.34±1.44	5.6 ± 4.5	6.25±0.75	0.16±0.03	5.6 ± 4.5	
J143218.26+430126.7	1396-53112-338	1.01 ± 0.00 ²	78.3 ± 90 ¹	1.48 ¹	-0.39±0.56	55.37 ± 81.19	1.5 MG, 90°
J143235.46+454852.5	1288-52731-449	12.29±6.98	50.62 ± 88.7	13.08±4.78	0.40±0.11	25.84 ± 33.41	10 MG, 30°
J144614.00+590216.7	608-52081-140	4.42±3.79	48.9 ± 31.58	2.18 ± 0.00 ²	0.40±0.26	4.72 ± 13.13	7 MG, 70°
J145415.01+432149.5	1290-52734-469	2.35±0.88	49.04 ± 17.87	2.15±1.09	0.27±0.11	53.38 ± 22.89	5 MG, ...
J150813.20+394504.9	1398-53146-633	13.23±3.11	37.55 ± 4.17	7.96±0.76	0.40±0.04	24.68 ± 5.61	20 MG, 90°
J151130.17+422023.0	1291-52735-612	22.40±9.41	48.6 ± 19.5	8.37±1.07	0.31±0.06	5.8 ± 21.1	12 MG, 60°
J151415.65+074446.5	1817-53851-534	35.34 ± 2.80	56.59 ± 17.23	35.88 ± 3.75	0.12 ± 0.043	56.08 ± 22.18	
J151745.19+610543.6	613-52345-446	13.98±7.36	60.07 ± 196.18	6.07±3.24	0.23±0.35	24.86 ± 47.72	17 MG, 30°
J152401.60+185659.2	2794-54537-410	11.96 ± 1.85	41.53 ± 8.79	10.27 ± 3.12	0.11 ± 0.02	33.40 ± 6.58	
J153532.25+421305.6	1052-52466-252	5.27±4.05	0.35 ± 41.68	9.05±5.27	-0.29 ± 0.12	0.13 ± 0.37	4.5 MG, 60°
J153829.29+530604.6	795-52378-637	13.99±3.82	48.96 ± 15.69	15.99±3.03	0.36±0.11	53.36 ± 29.05	12 MG, 30°
J153843.10+084238.2	1725 54266 297	13.20 ± 4.34	41.09 ± 90 ¹	9.63±	24.98 ± 34.53	0.33 ± 0.08	
J154213.48+034800.4	594-52045-400	8.35±2.60	54.34 ± 35.5	8.25±2.72	0.19±0.16	44.48 ± 30.63	8 MG, 60°
J154305.67+343223.6	1402-52872-145	4.09 ± 2.67	62.06 ± 158.24	4.02 ± 1.09	0.20 ± 0.06	62.67 ± 22.69	
J160437.36+490809.2	622-52054-330	59.51±4.64	40.83 ± 28.87	38.36±3.61	0.14±0.02	7.95 ± 10.24	53 MG, 0°
J164357.02+240201.3	1414-53135-191	2.00 ± 0.00 ²	88.01 ± 56.93	2.41±10.10	-0.34±0.99	18.54 ± 33.29	4 MG, 90°
J164703.24+370910.3	818-52395-026	2.10±0.67	68.39 ± 18.11	2.15±1.21	0.28±0.10	72.53 ± 18.41	2* MG, 90*°
J165029.91+341125.5	1175-52791-482	3.38±0.67	48.78 ± 13.64	3.92±1.05	0.40±0.12	57.74 ± 32.5	3* MG, 0*°
J165203.68+352815.8	820-52438-299	7.37±2.92	48.98 ± 11.77	9.53±3.53	0.40±0.08	51.15 ± 30.36	9.5 MG, 60°
J165249.09+333444.9	1175-52791-095	5.07 ± 4.18	54.25 ± 28.04	5.82 ± 1.90	0.39 ± 0.11	49.85 ± 36.73	
J170400.01+321328.7	976-52413-319	50.11±25.08	54.87 ± 118.04	56.16±8.84	0.27±0.05	0.34 ± 53.88	5 MG, 90*°
J171556.29+600643.9	354-51792-318	2.03 ± 0.00 ²	86.63 ± 31.39	2.03 ± 0.00 ²	-0.19±0.09	60.85 ± 35.29	4.5 MG, 60°
J172045.37+561214.9	367-51997-461	19.79±5.42	56.7 ± 21.33	9.72±2.68	0.31±0.18	0.85 ± 36.62	7 MG, 30°
J172329.14+540755.8	359-51821-415	32.85±3.56	37.43 ± 26.52	28.86±2.71	0.04±0.03	25.4 ± 27.51	35 MG, 10°
J172932.48+563204.1	358-51818-239	27.26±7.04	51.19 ± 67.41	27.17±18.71	0.22±0.10	41.74 ± 90 ¹	35 MG, ...
J202501.10+131025.6	2257-53612-167	10.10±1.76	68.5 ± 9.1	10.72±1.71	0.29±0.04	53.7 ± 9.0	
J204626.15-071037.0	635-52145-227	2.03 ± 0.00 ²	49.33 ± 25.34	2.62±0.53	0.40±0.06	54.97 ± 17.54	2 MG, 60°
J205233.52-001610.7	982-52466-019	13.42±3.73	68.57 ± 12.86	1.31±0.23	0.130.03	56.97 ± 16.83	13 MG, 80°
J214900.87+004842.8	1107-52968-374	10.09±4.71	46.97 ± 99.7	5.53±2.90	0.22±0.11	5.00 ± 9.13	10 MG, 60°
J214930.74-072812.0	644-52173-350	44.71±1.92	67.27 ± 26.38	44.71±2.80	0.06±0.05	60.11 ± 16.52	42 MG, 30°
J215148.31+125525.5	733-52207-522	20.76±1.39	68.3 ± 12.21	21.80±3.09	0.12±0.03	68.66 ± 19.04	21 MG, 90°

Table 2. continued.

MWD (SDSS+)	Plate-MJD-FiberID	B_p / MG	i / deg	B_{off} / MG	$z_{\text{off}} / r_{\text{WD}}$	i / deg	Comments
J220435.05+0012 42.9	372-52173-626	1.02±0.10	71.2 ± 90 ¹	2.50±5.47	-0.36±0.69	3.1 ± 13.6	
J221828.59-000012.2	374-51791-583	257.54 ± 48.71	17.68 ± 17.63	212.18 ± 34.78	0.06 ± 0.02	17.09 ± 27.01	225 MG, 30°
J224741.46+145638.8	740-52263-444	42.11 ± 2.83	53.02 ± 9.70	46.95 ± 4.30	-0.17 ± 0.02	33.16 ± 9.84	560 MG, ...
J225726.05+075541.7	2310-53710-420	16.17±2.81	74.9 ± 16.1	17.39±3.21	0.15±0.05	78.5 ± 34.8	
J231951.73+010909.3	382-51816-565	9.35±31.50	48.98 ± 11.36	6.06±1.24	0.40±0.09	12.48 ± 50.66	1.5* MG, 90*°
J232248.22+003900.9	383-51818-421	21.40±3.36	49.00 ± 15.42	21.65±4.48	0.29±0.07	44.174 ± 25.58	19 MG, 60°
J234605.44+385337.6	1883-53271-272	798.1 ± 163.6	2.50 ± 1.07	706.0 ± 238.9	0.12 ± 0.06	86.6 ± 15.4	1000* MG, ...
J234623.69-102357.0	648-52559-142	9.17±1.58	48.78 ± 9.62	2.25±0.29	0.39±0.07	8.42 ± 2.6	2.5 MG, 90*°

Asterisks indicate field strengths or inclinations with uncertainties greater than 10% in Vanlandingham et al. (2005).

¹ The errors are very large.

² The errors are very small.

Acknowledgements. Part of this work supported by the DLR under grant 50 OR 0201. The Sloan Digital Sky Survey (SDSS) is a joint project of the University of Chicago, Fermilab, the Institute for Advanced Study, the Japan Participation Group, the Johns Hopkins University, the Max-Planck-Institut für Astronomie, New Mexico State University, Princeton University, the United States Naval Observatory, and the University of Washington. Apache Point Observatory, site of the SDSS, is operated by the Astrophysical Research Consortium. Funding for the project has been provided by the Alfred P. Sloan Foundation, the SDSS member institutions, the National Aeronautics and Space Administration, the National Science Foundation, the U.S. Department of Energy, Monbusho, and the Max Planck Society. The SDSS World Wide Web site is <http://www.sdss.org/>.

B.K. would like to acknowledge support from the International Max-Planck Research School (IMPRS) for Astronomy and Cosmic Physics at the University of Heidelberg, and Heidelberg Graduate School of Fundamental Physics (HGSFP).

Vanlandingham, K. M., Schmidt, G. D., Eisenstein, D. J., et al. 2005, *AJ*, 130, 734
 Wickramasinghe, D. T. & Ferrario, L. 2000, *PASP*, 112, 873
 Wickramasinghe, D. T. & Ferrario, L. 2005, *MNRAS*, 356, 1576
 Zhang, E.-H., Robinson, E. L., & Nather, R. E. 1986, *ApJ*, 305, 740

References

- Aurière, M., Wade, G. A., Silvester, J., et al. 2007, *A&A*, 475, 1053
 Bagnulo, S., Landi degl'Innocenti, M., & Landi degl'Innocenti, E. 1996, *A&A*, 308, 115
 Bagnulo, S., Landi Degl'Innocenti, M., Landolfi, M., & Mathys, G. 2002, *A&A*, 394, 1023
 Bagnulo, S., Landstreet, J. D., Mason, E., et al. 2006, *A&A*, 450, 777
 Bergeron, P., Liebert, J., & Greenstein, J. L. 1990, *ApJ*, 361, 190
 Braithwaite, J. & Nordlund, Å. 2006, *A&A*, 450, 1077
 Braithwaite, J. & Spruit, H. C. 2004, *Nature*, 431, 819
 Burleigh, M. R., Marsh, T. R., Gänsicke, B. T., et al. 2006, *MNRAS*, 373, 1416
 Debes, J. H., López-Morales, M., Bonanos, A. Z., & Weinberger, A. J. 2006, *ApJ*, 647, L147
 Donati, J. F., Achilleos, N., Matthews, J. M., & Wesemael, F. 1994, *A&A*, 285, 285
 Euchner, F., Jordan, S., Beuermann, K., Gänsicke, B. T., & Hessman, F. V. 2002, *A&A*, 390, 633
 Euchner, F., Jordan, S., Beuermann, K., Reinsch, K., & Gänsicke, B. T. 2006, *A&A*, 451, 671
 Euchner, F., Reinsch, K., Jordan, S., Beuermann, K., & Gänsicke, B. T. 2005, *A&A*, 442, 651
 Farihi, J., Burleigh, M. R., & Hoard, D. W. 2008, *ApJ*, 674, 421
 Friedrich, S., Ostreicher, R., Ruder, H., & Zeller, G. 1994, *A&A*, 282, 179
 Fukugita, M., Ichikawa, T., Gunn, J. E., et al. 1996, *AJ*, 111, 1748
 Gänsicke, B. T., Euchner, F., & Jordan, S. 2002, *A&A*, 394, 957
 Gänsicke, B. T., Schmidt, G. D., Jordan, S., & Szkody, P. 2001, *ApJ*, 555, 380
 Harris, H. C., Liebert, J., Kleinman, S. J., et al. 2003, *AJ*, 126, 1023
 Holberg, J. B. & Bergeron, P. 2006, *AJ*, 132, 1221
 Jordan, S. 1992, *A&A*, 265, 570
 Jordan, S. 2001, in *Astronomical Society of the Pacific Conference Series*, Vol. 226, 12th European Workshop on White Dwarfs, ed. J. L. Provencal, H. L. Shipman, J. MacDonald, & S. Goodchild, 269–+
 Jordan, S. 2009, ArXiv e-prints
 Jordan, S. & Schmidt, H. 2003, in *Astronomical Society of the Pacific Conference Series*, Vol. 288, *Stellar Atmosphere Modeling*, ed. I. Hubeny, D. Mihalas, & K. Werner, 625–+
 Kawka, A., Vennes, S., Schmidt, G. D., Wickramasinghe, D. T., & Koch, R. 2007, *ApJ*, 654, 499
 Kleinman, S. J., Harris, H. C., Eisenstein, D. J., et al. 2004, *ApJ*, 607, 426
 Landolfi, M., Bagnulo, S., & Landi degl'Innocenti, M. 1998, *A&A*, 338, 111
 Latter, W. B., Schmidt, G. D., & Green, R. F. 1987, *ApJ*, 320, 308
 Liebert, J., Bergeron, P., & Holberg, J. B. 2003, *AJ*, 125, 348
 Liebert, J., Bergeron, P., Schmidt, G. D., & Saffer, R. A. 1993, *ApJ*, 418, 426
 Muslimov, A. G., van Horn, H. M., & Wood, M. A. 1995, *ApJ*, 442, 758
 Putney, A. 1995, *ApJ*, 451, L67+
 Rechenberg, I. 1994, *Werkstatt Bionik und Evolutionstechnik No. 1* (Stuttgart: frommann-holzboog
 Reimers, D., Jordan, S., Beckmann, V., Christlieb, N., & Wisotzki, L. 1998, *A&A*, 337, L13
 Schmidt, G. D., Harris, H. C., Liebert, J., et al. 2003, *ApJ*, 595, 1101
 Schmidt, G. D., Szkody, P., Silvestri, N. M., et al. 2005, *ApJ*, 630, L173
 Schmidt, G. D., Vennes, S., Wickramasinghe, D. T., & Ferrario, L. 2001, *MNRAS*, 328, 203
 Schmidt, G. D., West, S. C., Liebert, J., Green, R. F., & Stockman, H. S. 1986, *ApJ*, 309, 218
 Shorlin, S. L. S., Wade, G. A., Donati, J.-F., et al. 2002, *A&A*, 392, 637
 Stoughton, C., Lupton, R. H., Bernardi, M., et al. 2002, *AJ*, 123, 485
 Tillich, A., Geier, S., Heber, U., et al. 2009, ArXiv e-prints; arXiv:0901.1030
 Tout, C. A., Wickramasinghe, D. T., Liebert, J., Ferrario, L., & Pringle, J. E. 2008, *MNRAS*, 387, 897

Appendix A: Figures of all fits not shown in the printed version

The full preprint version can download from http://www.ari.uni-heidelberg.de/mitarbeiter/bkulebi/papers/12570_online.pdf.